

CrossMark
click for updatesCite this: *J. Mater. Chem. A*, 2016, 4, 12638

Multigrain electrospun nickel doped lithium titanate nanofibers with high power lithium ion storage†

Salah Abureden, Fathy M. Hassan, Gregory Lui, Wook Ahn, Serubbabel Sy, Aiping Yu and Zhongwei Chen*

Novel *in situ* nickel doped 1-D lithium titanate nanofibers ($\text{Li}_4\text{Ti}_{5-x}\text{Ni}_x\text{O}_{12}$, where $x = 0, 0.05$ and 0.1) have been successfully synthesized using a facile electrospinning process. Physical characterization reveals that nickel is homogeneously incorporated into the lattice of lithium titanate nanofibers (LTONFs) which significantly improves their properties yielding outstanding electrochemical performance in a lithium ion battery at high power rates and significant reduction in the voltage gap between the oxidation and reduction peaks. A capacity of 190 mA h g^{-1} has been obtained at 0.2C for the 10% nickel doped nanofibers (Ni-LTONF₁₀), which is higher than the theoretical capacity of pristine lithium titanate (175 mA h g^{-1}) and they also show superior rate capability resulting in 63 mA h g^{-1} obtained at 50C , which is 20 times higher than that of un-doped pristine LTONFs and lithium titanate nanoparticles (LTONPs). Finally, a hybrid supercapacitor is fabricated using Ni-LTONF₁₀, showing superior energy density at high power density.

Received 15th May 2016

Accepted 4th July 2016

DOI: 10.1039/c6ta04046b

www.rsc.org/MaterialsA

Introduction

The development of portable electronics, electric vehicles, and smart grids is increasing the need for reliable energy storage devices with safe operation and high power capabilities.^{1,2} Lithium ion batteries (LIBs) have been studied extensively in the past few years as one of the most promising candidates for these applications. However, the current graphite-based electrode technologies used in LIBs suffer from limited power capabilities and safety concerns.³ To address these challenges, researchers have investigated a number of alternative materials. Spinel lithium titanate (LTO) is one such material that is chosen for its safety, high power density, and rate capability which stem from its outstanding ability to accommodate lithium ions without a significant structural change during charge and discharge operations (zero-strain).^{4,5} The theoretical capacity of LTO is 175 mA h g^{-1} with a stable plateau at $1.55 \text{ V versus Li/Li}^+$. This relatively high voltage minimizes the chance of lithium dendrite formation and electrolyte decomposition which usually occur at lower voltages, causing cell failure and possibly fire due to cell overheating. Although LTO has remarkable characteristics, its electrochemical performance and practical applications are still limited due to its poor electronic conductivity and low energy density.⁶ Different approaches have been investigated to

overcome these limitations such as carbon coating, particle size reduction, and transition metal doping.^{3,4} Carbon coating improves the conductivity and rate capability of LTO, while particle size reduction shortens the lithium diffusion path which improves intercalation kinetics and improves battery capacity.⁴ Doping with transition metals has been found to enhance conductivity and lithium ion diffusivity leading to higher capacity and improved rate capability.⁷ Research studies on metal doping have been focused mainly on lithium titanate nanoparticles (LTONPs), nanowires, and nanotubes.^{8–16}

Nickel is a highly abundant and inexpensive dopant that has the potential to improve the performance of LTO-based LIBs. Investigations on nickel doped LTO nanoparticles were conducted in the past. In some studies, nickel doped LTO nanoparticles were found to increase the initial capacity of the battery.^{17,18} Other studies found marginal improvement in the rate capability performance of nickel doped LTO nanoparticles synthesized using different methods, including hydrothermal and solid state reactions.^{5,19} Co-doping LTO with nickel and manganese was reported to improve capacity and cycling performance.²⁰ These investigations led to the development of advanced LTO materials. However, their improvements were incremental and no remarkable combined advancements in both rate capability and energy density have been reported yet.

On the other hand, 1D nanofibers are very attractive because they can be easily produced by low cost and facile electrospinning, which makes the electrospun nanofibers highly scalable for large batch production. The principle of electrospinning is based on applying a high voltage between an

Chemical Engineering Department, University of Waterloo, 200 University Ave., Waterloo, Ontario, N2L 3G1, Canada. E-mail: zhwen@uwaterloo.ca

† Electronic supplementary information (ESI) available. See DOI: 10.1039/c6ta04046b

injected solution droplet and an opposing collector. Charge accumulation on the droplet surface causes electrostatic repulsion with the surface tension force which stretches the droplet to form what is known as the Taylor cone.²¹ When the applied voltage reaches a critical value, the force of the electric field overcomes the surface tension force and the fiber jet elongates and is deposited on the collector. Electrospinning is affected by a number of parameters, including the solution viscosity and concentration, applied voltage, flow rate, solution conductivity, and the distance between the needle tip and the collector. The main advantages of electrospinning are the low cost, scalability, simplicity of the experimental setup, the high surface area and small pore size of the fibers that can be synthesized. The main disadvantages of electrospinning are the difficulty in obtaining uniform thickness of the fibers, fiber disruption, and the formation of large beads.^{22,23} In this work, we used a sufficiently viscous PVP precursor solution and optimized the experimental parameters as explained in the Experimental section to overcome these disadvantages.²⁴

The 1D nanofibers can be a very good choice for LIB applications because 1D nanofibers show good strain relaxation, shorter Li⁺ diffusion paths, interfacial control, and continuous electron transport pathways, which are all very favorable for improving the LIB performance.^{3,25–28} A number of studies reported using 1D nanofibers in LIBs;^{29–31} however, nickel doping into LTO one-dimensional nanofibers has not yet been investigated and reported in the literature.³² In this work, we report successful *in situ* doping of nickel into 1D lithium titanate nanofibers (LTONFs) using a facile and scalable electrospinning technique followed by a heat treatment. We investigated three Ni to LTO molar ratios: 0%, 5% and 10%. It is worth mentioning that the 15% doping ratio was not possible with similar electrospinning parameters to the three other doping ratios. This can be attributed to the effect of the additional nickel on the precursor solution conductivity and charge density at the surface of the injected solution droplet. Increasing the nickel amount increases the solution conductivity and charge density beyond the critical value, which hinders the creation of the Taylor cone required to initiate the elongation of fiber jets.^{33,34}

Our strategy in this work reporting nickel doping into LTO nanofibers for the first time is based on dual improvements of both electronic conductivity and lithium diffusivity of LTO in order to simultaneously enhance rate capability as well as energy density of the LIB. The advantage of our approach is the simplicity and unique coupling of *in situ* nickel doping distributed homogeneously into the stable 1D LTO nanofiber lattice. The obtained promising results can open the door for more research on the use of nanofibers for LIB applications. A performance comparison of nickel doped LTO nanofibers with previous studies is shown in Table S1 in the ESI.†

The pure LTONF sample with $x = 0$ is referred to as LTONF, the sample with $x = 0.05$ is referred to as Ni-LTONF₅, and for $x = 0.1$, the sample is referred to as Ni-LTONF₁₀, while LTO nanoparticles are referred to as LTONPs.

Results and discussion

Characterization

The XRD patterns of all samples are shown in Fig. 1a; the results show that all patterns are almost identical. The sharp diffraction peaks located at $2\theta = 18.6^\circ$, 37° , 43° , 58° , and 63° correspond to (111), (311), (400), (511), (440), and (531) planes, respectively. These peaks represent single phase spinel LTO with the *Fd3m* space group (JCPDS card number 49-0207) which reveals that calcination at 780°C in air leads to well crystallized LTO with no indication of impurities. The crystallization process has significant effects on LIB performance because crystallinity and material purity affect both lithiation kinetics and lithiation capacity. Studies have shown that the initial crystallinity of TiO₂ can have an effect on the crystallization and purity of Li₄Ti₅O₁₂.^{35,36} Amorphous materials tend to hinder lithiation because of their disordered structure, while crystalline materials allow more facile lithiation.³⁶ The as-synthesized TiO₂ nanofibers are structurally amorphous as they were prepared at room temperature by the hydrolysis of titanium isopropoxide. Heat treatment of amorphous TiO₂ will form a crystalline phase of TiO₂ which will then undergo solid-state

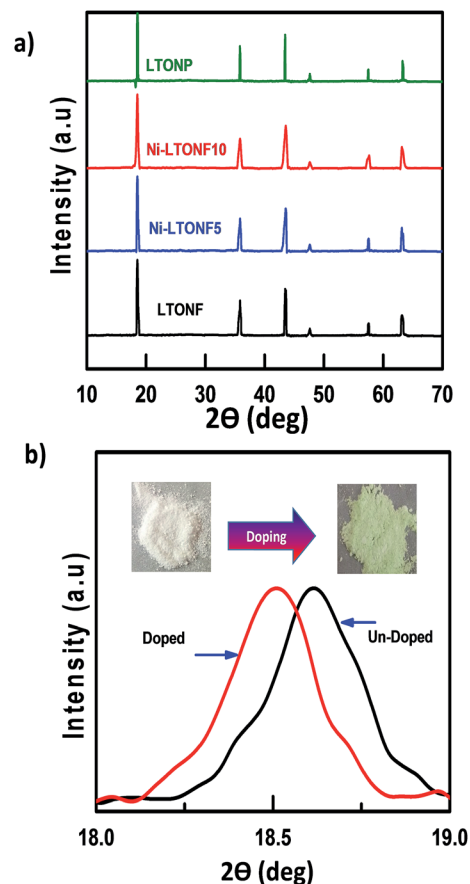


Fig. 1 (a) XRD patterns of LTONPs, LTONFs, Ni-LTONF₅, and Ni-LTONF₁₀ and (b) magnification of the XRD peak corresponding to the (111) plane of LTONFs and Ni-LTONF₁₀ showing a negative peak shift due to nickel doping. The inset shows optical images of LTO nanofibers before and after doping.

conversion to the crystalline phase of $\text{Li}_4\text{Ti}_5\text{O}_{12}$ via lithiation by the lithium source.^{35,36} The similarity in XRD patterns of doped and pure samples also indicates that nickel doping has not obviously changed the crystal structure of LTONFs. However, broader peaks are found in LTONF, Ni-LTONF₅, and Ni-LTONF₁₀ XRD patterns compared to the LTONP XRD pattern. This difference is attributed to the crystal refinement of the nanofiber samples resulting from a difference in the synthesis method. To verify the doping effect of nickel, the specific peak corresponding to the (111) plane of LTONFs and Ni-LTONF₁₀ is magnified and shown in Fig. 1b. Ni-LTONF₁₀ shows a slight shift in the diffraction peak of the (111) plane to a lower angle ($2\theta = 18.51^\circ$) compared to the diffraction peak of pure LTONFs ($2\theta = 18.6^\circ$). This decrease indicates that the lattice parameter of Ni-LTONF₁₀ is slightly higher than that of pure LTONFs. This is attributed to the size of nickel (0.69 Å) being slightly larger than that of titanium (0.60 Å).^{10,19,37} The shift in the diffraction peak is additional evidence for the successful doping of nickel which can also be observed in the change of the color of the end product, as seen in the inset of Fig. 1b.

The lattice parameters of the pure and doped LTO nanofibers are calculated by mathematical calculations using the following equations^{38,39}

$$2d(\sin \theta) = n\lambda \quad (1)$$

$$1/d^2 = (h^2 + k^2 + l^2)/a^2 \quad (2)$$

where d is the distance between the atomic layers, θ is the beam angle, n is the integer number of wavelengths (1), and λ is the wavelength of the incident beam. h , k , and l are Miller indices and a is the lattice parameter. The lattice parameters are found to be 8.366 Å, 8.373 Å and 8.379 Å for LTONFs, Ni-LTONF₅ and Ni-LTONF₁₀, respectively. The slight increase in the lattice parameter with increasing doping percentage is attributed to the slight expansion of the lattice due to the partial substitution of titanium with nickel which is also confirmed by XPS results.

X-ray photoelectron spectroscopy (XPS) was utilized to investigate the material composition before and after nickel doping of LTONFs. Fig. 2a shows the general XPS spectra of three LTO nanofiber samples, while Fig. 2b shows magnification of the XPS Ti 2p peaks. The un-doped LTONF shows two peaks at 458.54 eV and 464.31 eV corresponding to the $2p_{1/2}$ and $2p_{3/2}$ peaks of Ti^{4+} . The peaks were shifted to a lower energy level after nickel doping with 458.21 eV and 463.91 eV for Ni-LTONF₅ and 458.07 eV and 463.82 eV for Ni-LTONF₁₀ which reveal the effect of nickel doping on changing the valence state of Ti ions from Ti^{4+} to Ti^{3+} leading to enhanced electrochemical properties well documented in the literature.^{15,40,41}

The composition change of the LTO nanofibers before and after doping is summarized in Table 1. The results reveal that nickel doping causes the formation of $\text{Li}_4\text{Ti}_{5-x}\text{Ni}_x\text{O}_{12}$ ($x = 0.05$ and 0.1) which explains the capacity increase of doped LTO at low current density compared to un-doped LTO.

The BET analysis of the three LTO nanofiber samples was carried out. Fig. 3 shows the nitrogen adsorption/desorption isotherm curves and the pore size distribution. The surface

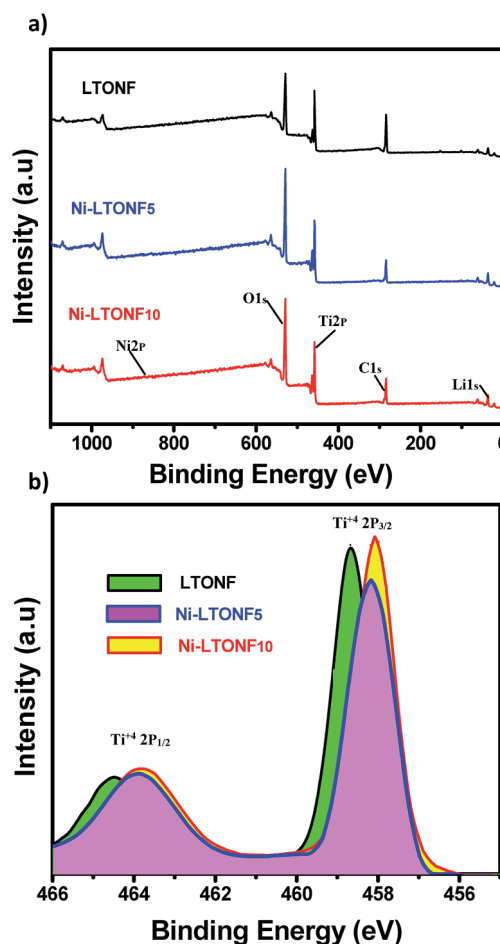


Fig. 2 (a) General XPS spectra of LTONFs, Ni-LTONF₅ and Ni-LTONF₁₀ and (b) magnification of XPS Ti 2p peaks of LTONFs, Ni-LTONF₅ and Ni-LTONF₁₀.

Table 1 Elemental composition (atomic percentage) of the LTO nanofiber samples

	LTONF	Ni-LTONF ₅	Ni-LTONF ₁₀
Lithium%	19.28	19.047	19.02
Titanium%	22.75	23.57	23.23
Oxygen%	57.97	57.14	57.06
Nickel%	0	0.24	0.49

areas of the three samples are found to be almost similar, with surface areas of 8.22, 8.55 and 7.96 $\text{m}^2 \text{g}^{-1}$ for LTONFs, Ni-LTONF₅, and Ni-LTONF₁₀, respectively. The average pore size diameters are found to be 5.9, 8.5 and 7.6 nm for LTONFs, Ni-LTONF₅, and Ni-LTONF₁₀, respectively. The similarities in the surface area and pore size are more indications that the improvement in electrochemical performance is mainly driven by nickel doping.

The SEM images of LTONFs and Ni-LTONF₁₀ before and after calcination in addition to LTONPs are shown in Fig. 4. The nanofiber samples show a continuous, fibrous morphology,

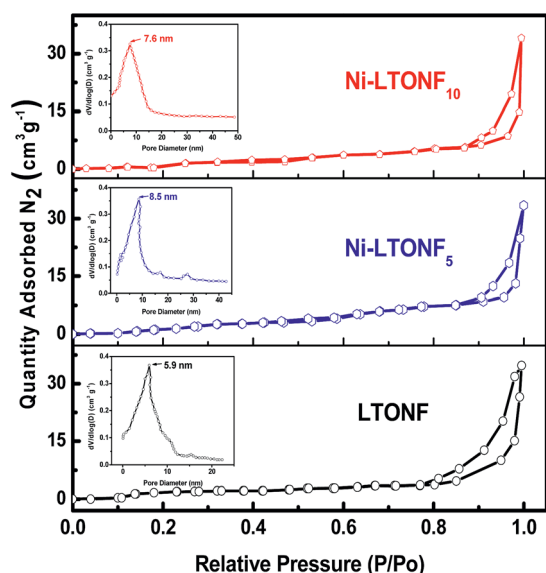


Fig. 3 Nitrogen adsorption/desorption isotherm curves and the pore size distribution curves (inset).

with a diameter in the range of 700–800 nm before calcination and 300–400 nm after calcination. This reduction in diameter is due to the removal of PVP. The diameter of Ni-LTONF₁₀ is in the range of 750–850 nm before calcination which is reduced to 350–450 nm after calcination. The diameter of Ni-LTONF₁₀ before and after calcination maintained an average range of 50–100 nm difference in diameter compared to that of LTONFs. Furthermore, both of the materials after calcination show homogeneous surface roughness, indicating that the granular-like structure of primary nanoparticles of LTONFs maintains a fiber-like structure. This 1D nanofiber structure obtained after calcination at 780 °C is suitable for excellent lithium ion diffusion and electrical conductivity as demonstrated by significantly enhanced LIB performance shown later. The SEM images of LTONPs confirm the nanoparticle morphology with a particle size range of 100–250 nm.

The TEM image of Ni-LTONF₁₀ in Fig. 5a shows the 1D morphology with aligned multigrains of nanoparticles. The lattice fringe fingerprint of HRTEM shown in Fig. 5b indicates the crystalline structure of Ni-LTONF₁₀ with a preferential orientation to the (111) plane. The polycrystalline structure of the material is revealed in the SAED pattern shown in Fig. 5c.

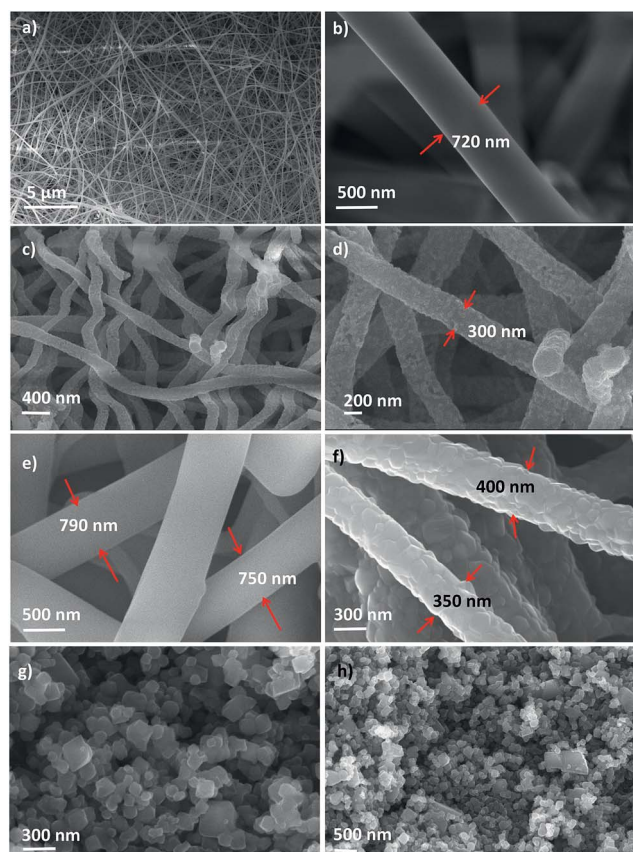


Fig. 4 (a and b) SEM images of electrospun LTONFs before heat treatment at low and high magnifications, (c and d) SEM images of the LTONF after heat treatment at low and high magnifications, (e and f) high magnification SEM images of Ni-LTONF₁₀ before and after heat treatment and (g and h) SEM images of LTONPs after heat treatment.

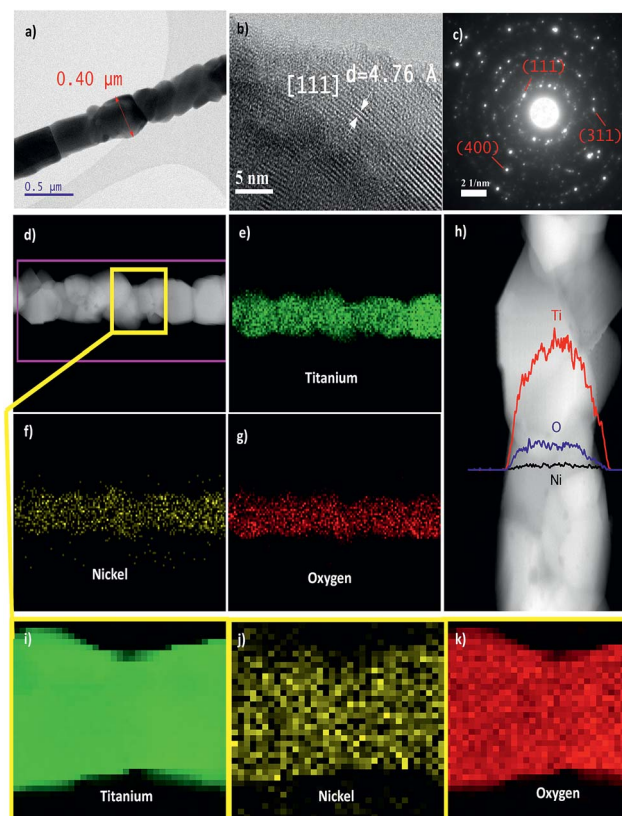


Fig. 5 (a) TEM image of Ni-LTONF₁₀, (b) high resolution TEM image of Ni-LTONF₁₀, (c) selected area electron diffraction pattern of Ni-LTONF₁₀, (d) HAADF-STEM image of Ni-LTONF₁₀, (e–g) EDS mapping of the nanofiber in (d) showing the elements titanium, nickel and oxygen, respectively, (h) EDS line scan showing the element profile across Ni-LTONF₁₀, and (i–k) electron energy loss spectroscopy mapping of the labelled part in (d) showing the elements titanium, nickel and oxygen, respectively.

The EDS images shown in Fig. 5d–g are based on high angle annular dark-field scanning transmission electron microscopy (HAADF-STEM) of one nanofiber. Both EDS elements mapping shown in Fig. 5e–g and EDS line scan shown in Fig. 5h clearly confirm the homogenous distribution of nickel into the lattice of LTO. Electron energy loss spectroscopy (EELS) is a technique that shows atomic resolution of the elemental composition. The EELS mapping for part of the wire in Fig. 5d is shown in Fig. 5i–k, further confirming the uniform distribution of nickel into the lattice of LTO (each pixel in these figures is equivalent to $6 \text{ nm} \times 6 \text{ nm}$).

Electrochemical performance

The LIB low current density charge–discharge tests were carried out in a potential range of 1–2.5 V at room temperature at 0.2C rate as shown in Fig. 6a. The LTONP has an energy capacity of 129 mA h g^{-1} while the pure LTONF shows 149 mA h g^{-1} reversible capacity. Ni-LTONF₅ shows a higher capacity of 164 mA h g^{-1} while Ni-LTONF₁₀ shows excellent improvement with 190 mA h g^{-1} reversible capacity which is not only higher than that of the LTONP, LTONF, and Ni-LTONF₅, but also

higher than the theoretical capacity of LTO (175 mA h g^{-1}). Fig. 6b shows the cyclic voltammetry test which was done in a voltage window of 1–2.5 V and at a scan rate of 0.5 mV s^{-1} for the 1D LTO electrospun samples to identify the change in redox behavior due to nickel doping. LTO is known to have a reduction peak at around 1.4 V and an oxidation peak around at 1.7 V. The experimental results of LTONFs show reduction and oxidation peaks similar to the standard LTO peaks indicating high crystallinity of the prepared sample.

Increasing nickel doping causes changes in the redox behavior of the tested materials. The oxidation peaks of the three materials are located at 1.71 V, 1.67 V, and 1.625 V and the reduction peaks are located at 1.43 V, 1.53 V, and 1.52 V for the LTONF, Ni-LTONF₅, and Ni-LTONF₁₀, respectively. Table 2 shows the voltage hysteresis (ΔV) between the reduction and oxidation peaks of the three samples. Ni-LTONF₅ shows 50% reduction in ΔV compared to the LTONF while Ni-LTONF₁₀ shows outstanding reduction in voltage hysteresis with a value three times smaller than that of the LTONF and sharper redox peaks. These changes indicate improved lithium diffusion kinetics due to the significant reduction in electrode polarization which allows for a much faster rate in lithium uptake and release.^{18,42,43}

Fig. 7 shows the rate capability tests of the LTONP, LTONF, Ni-LTONF₅ and Ni-LTONF₁₀ evaluated in the potential range of 1–2.5 V at room temperature using different current densities. The capacity fading for LTONPs was very fast with increasing C rates, showing only 25 mA h g^{-1} at 5C only and below 5 mA h g^{-1} at 20C, the capacity approached zero at C rates higher than 20C. LTONFs also suffered from fast capacity fading as LTONPs but

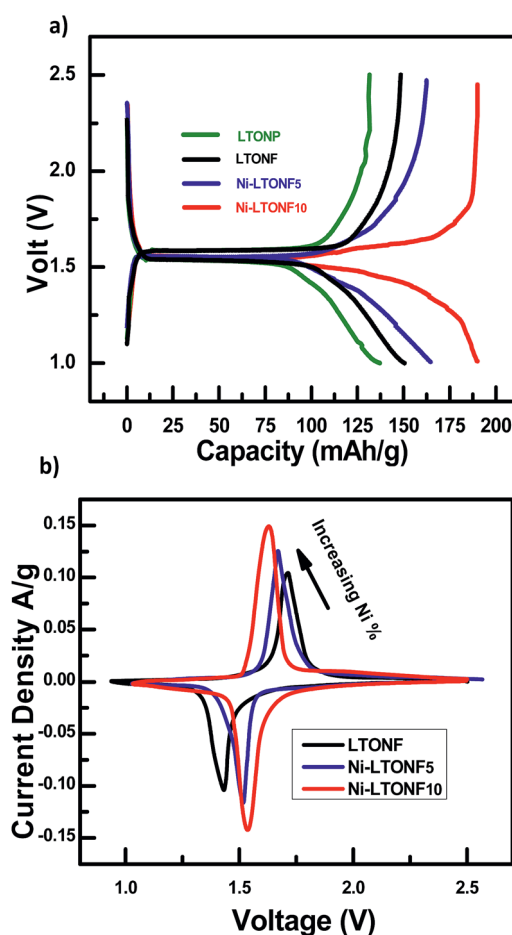


Fig. 6 (a) Galvanostatic charge–discharge profiles of the LTONP, LTONF, Ni-LTONF₅, and Ni-LTONF₁₀. (b) Cyclic voltammetry showing changes in redox behavior of the LTO nanofiber materials with the increase in nickel doping.

Table 2 The oxidation and reduction peaks of the three samples with the calculated voltage hysteresis

	Oxidation	Reduction	ΔV
LTONF	1.71	1.43	0.29
LTONF ₅	1.67	1.53	0.14
LTONF ₁₀	1.62	1.52	0.1

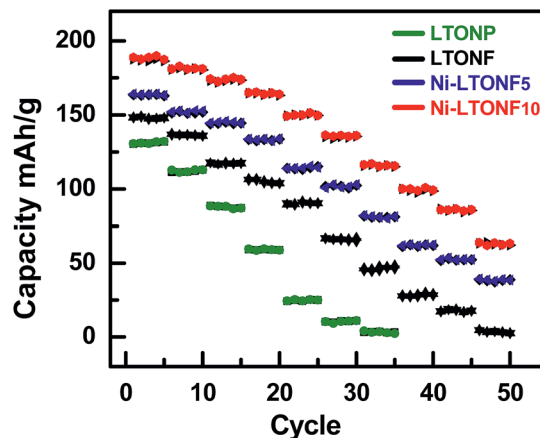


Fig. 7 Rate capability of the LTONP, LTONF, Ni-LTONF₅ and Ni-LTONF₁₀ measured at different current densities.

with a better performance of 48 mA h g^{-1} at 20C and below 5 mA h g^{-1} at 50C. Ni-LTONF₅ showed improved performance compared to the LTONP and LTONF with 81 mA h g^{-1} at 20C and 38 mA h g^{-1} at 50C. Finally, Ni-LTONF₁₀ showed outstanding rate capability performance at high C rates with 116 mA h g^{-1} at 20C and 63 mA h g^{-1} at 50C.

A comparison between the performance of the LTONF and Ni-LTONF₁₀ at low and high C rates is shown in Fig. 8a. The result shows that the performance of Ni-LTONF₁₀ at 50C is 20 times higher than that of the LTONF. Fig. 8b shows a comparison of the discharge capacity values of the 1D nanofiber LTO

materials at different C rates as a function of their discharge capacities at 0.2C. The results prove that Ni-LTONF₁₀ maintains higher values at all C rates.

For further investigation on the effect of nickel doping on the durability and cycling behavior of the 1D nanofiber materials, the long-term cycling performance was evaluated at 10C as shown in Fig. 8c. The LTONF retains a discharge capacity of 57 mA h g^{-1} after 1000 cycles which corresponds to 85% of the first discharge capacity (67 mA h g^{-1}). Ni-LTONF₅ maintains 90.6 mA h g^{-1} discharge capacity, corresponding a capacity retention of 89% ($101.8 \text{ mA h g}^{-1}$). Ni-LTONF₁₀ shows the highest performance after 1000 cycles with $126.8 \text{ mA h g}^{-1}$ discharge capacity corresponding to a capacity retention of 94% ($134.9 \text{ mA h g}^{-1}$) and an average capacity loss per cycle equivalent to $8.09 \times 10^{-3} \text{ mA h g}^{-1}$.

2D Raman mapping was utilized to investigate the stability of the 1D nanofiber morphology of the un-doped LTONF and Ni-LTONF₁₀ before and after long-term cycling at a high power rate (10C). Fig. 9a and b show the un-doped nanofibers before cycling at the electrode surface and at $10 \mu\text{m}$ depth, respectively, while Fig. 9c and d show the un-doped nanofibers at the surface and at $10 \mu\text{m}$ depth after long-term cycling. Fig. 9e and f show Ni-LTONF₁₀ nanofibers before cycling at the electrode surface and at $10 \mu\text{m}$ depth. Fig. 9g and h show Ni-LTONF₁₀ nanofibers at the surface and at $10 \mu\text{m}$ depth after long-term cycling. The results show that 1D longitudinal nanofiber morphology was not damaged after long-term cycling for both doped and un-doped samples. The stable morphology of both electrode materials after long-term cycling at the surface and at the deepest point of the electrode indicates that the difference in the ability to maintain improved electrochemical performance between doped and un-doped samples is not attributed to the morphological change or electrode deterioration of the LTONF from long-term cycling at 10C but rather to the effect of nickel on enhancing lithium intercalation thermodynamics for LTONF₁₀.

Electrochemical impedance spectroscopy (EIS) was employed to understand the effect of nickel doping on the lithium diffusivity and electrical conductivity. Fig. 10a shows the Nyquist plot of the impedance spectra for the three LTO nanofiber materials. All plots have a semicircle in the high frequency region and a straight line in the low frequency zone. The low frequency zone is attributed to the diffusion of the lithium ions into the bulk of the electrode. Fig. 10b shows the relationship between real impedance and the reciprocal square root of the lower angular frequencies $\omega^{-0.5}$. Lithium diffusion coefficients are calculated based on the following equations^{44,45}

$$Z_{\text{re}} = R_s + R_{\text{ct}} + \sigma_w \omega^{-0.5} \quad (3)$$

$$D = 0.5(RT/An^2F^2\sigma_w C)^2 \quad (4)$$

where R_s is the electrolyte resistance, R_{ct} is the charge transfer resistance at the surface of the active material, σ_w is the Warburg impedance coefficient ($\Omega \text{ s}^{-0.5}$), ω is the angular frequency in the low frequency region ($\omega = 2\pi f$), D is the diffusion coefficient, R is the gas constant, T is the absolute temperature, F is

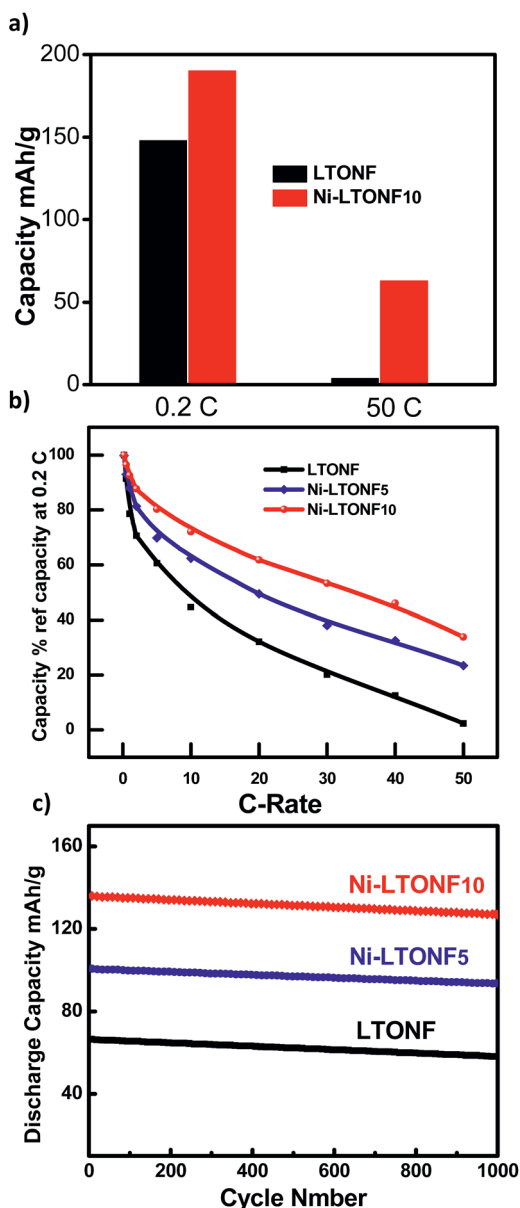


Fig. 8 (a) The performance of the LTONF and Ni-LTONF₁₀ at 0.2C and 50C showing the significant improvement of nickel doping at high C rates. (b) Rate performance of the LTONF, Ni-LTONF₅, and Ni-LTONF₁₀ at different C rates normalized to capacity at 0.2C. (c) Long-term cycling performance (1000 cycles) of the LTONF, Ni-LTONF₅, and Ni-LTONF₁₀ at 10C current density.

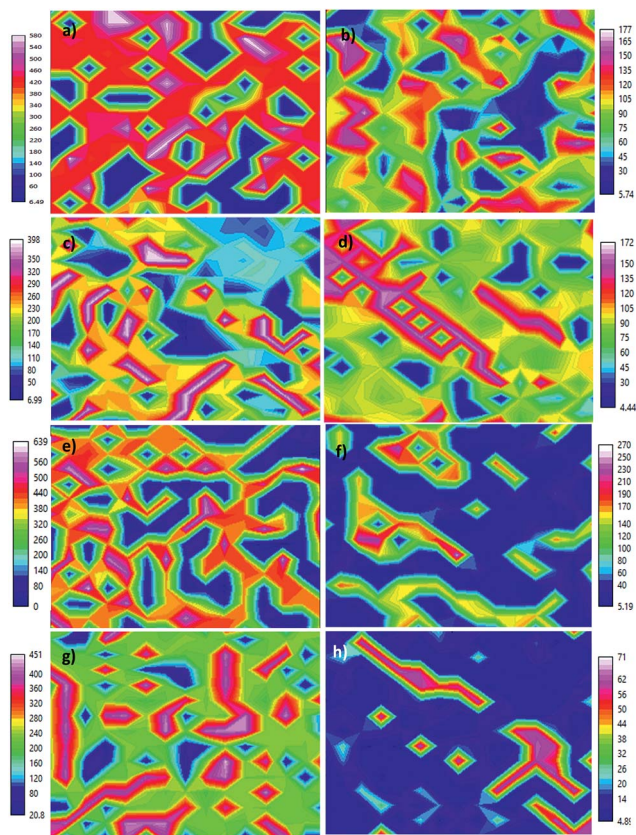


Fig. 9 2D Raman mapping of LTONF and Ni-LTONF₁₀ electrodes, (a and b) LTONF before cycling at the surface and at 10 μm, respectively, (c and d) LTONF after cycling at the surface and 10 μm, respectively, (e and f) Ni-LTONF₁₀ before cycling at the surface and at 10 μm, respectively and (g and h) Ni-LTONF₁₀ after cycling at the surface and at 10 μm, respectively.

Faraday's constant, A is the area of the electrode surface, and C is the molar concentration of Li^+ ions in 1 cm^3 .

Table 3 shows a summary of the calculated values of R_s , R_{ct} , σ_w and D . Ni-LTONF₁₀ shows $5.86 \times 10^{-12} \text{ cm}^2 \text{ s}^{-1}$ which is significantly higher (17 times) than that of pure LTO ($3.43 \times 10^{-13} \text{ cm}^2 \text{ s}^{-1}$). The results clearly show the effect of nickel doping on improving the lithium diffusion coefficient and enhancing the overall electrochemical performance of the LTO nanofibers.⁴⁵

For further investigation, we fabricated an asymmetric hybrid supercapacitor (HSC) cell made of the Ni-LTONF₁₀ material as the anode and commercial activated carbon (AC) as the cathode. The mass ratio of the Ni-LTONF₁₀ to AC was 1 : 3 to balance the kinetics of the non-faradic and faradic components of the HSC as described in the below equations:

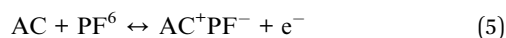


Fig. 11a shows the charge/discharge profiles of the HSC in a voltage window of 0–3 V measured at different current densities. All the curves show a change in the voltage charge/discharge rates with a gradual slope between 2 V and 3 V and

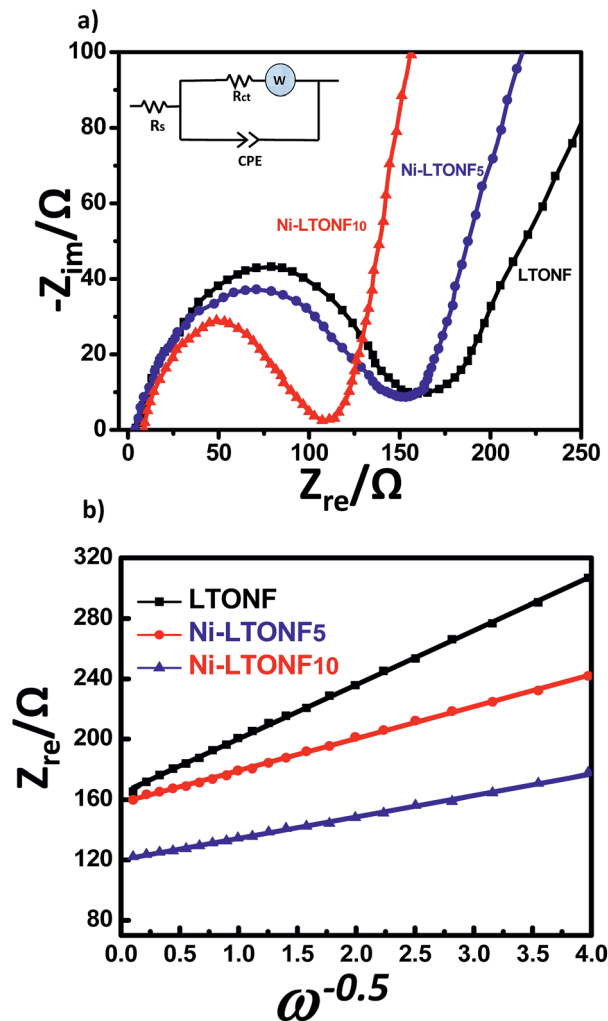


Fig. 10 (a) Nyquist plots of the LTONF, Ni-LTONF₅ and Ni-LTONF₁₀ measured before cycling with the equivalent circuit shown in the inset, and (b) the relationship between real impedance and $\omega^{-0.5}$.

Table 3 EIS parameters of the three LTO nanofiber samples

	LTONF	Ni-LTONF ₅	Ni-LTONF ₁₀
R_s (Ω)	4.26	4.18	5.317
R_{ct} (Ω)	160.1	153.08	114.29
σ_w ($\Omega \text{ s}^{-0.5}$)	35.91	21.2	14.22
D ($\text{cm}^2 \text{ s}^{-1}$)	3.43×10^{-13}	9.67×10^{-13}	5.86×10^{-12}

a sharper slope below 2 V which is attributed to the difference in charge/discharge kinetics between the battery portion of the HSC and the electrical double layer capacitor (EDLC) portion. The faradic Li^+ intercalation/de-intercalation reaction at the anode side happens concurrently with PF_6 double layer creation at the surface of both electrodes, causing a gradual slope in the region (2–3) V.

Fig. 11b shows the Ragone plot obtained from the discharge data in the voltage profile of the HSC measurement shown in Fig. 11a at different current densities using the following equations:^{46,47}

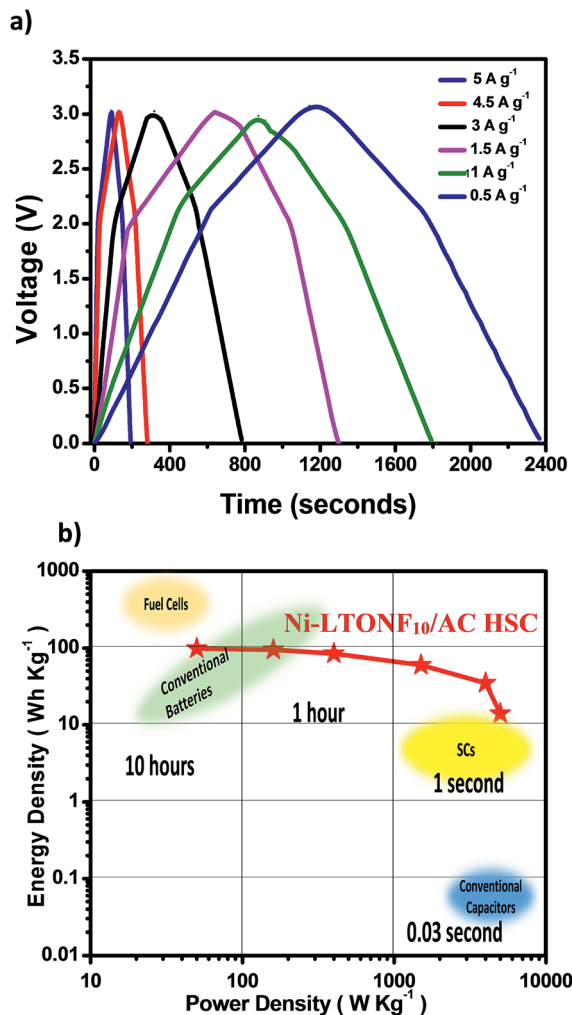


Fig. 11 (a) Charge/discharge profiles of the HSC in a voltage window of 0–3 V measured at different current densities and (b) Ragone plot obtained from the discharge part in the voltage profile of the HSC measurement at different current densities shown in (a).

$$E = 0.5C\Delta V^2 \quad (7)$$

$$P = E/dt \quad (8)$$

$$C = Idt/m\Delta V \quad (9)$$

where E is the energy density, C is the cell capacitance, ΔV is the potential window, P is the power density, dt is the discharge time and m is the total mass of active materials in both the anode and cathode.

The results clearly show that the hybridized supercapacitor has improved energy density at high power rates due to the additional faradaic reactions, improved conductivity and stability of the 1D Ni-LTONF₁₀ anode material.

All the improvements in electrochemical results shown in the previous results for the nickel doped LTO nanofiber material are attributed to the compositional change that happens to the LTO nanofibers due to the insertion of nickel into its lattice without a noticeable effect on its structure in the formation of

$\text{Li}_4\text{Ti}_{5-x}\text{Ni}_x\text{O}_{12}$ ($x = 0, 0.05$ and 0.1). LTO has a $Fd3m$ space group with the 8a tetrahedral sites occupied by lithium ions, 16d octahedral sites shared between lithium ions and titanium ions (Ti^{4+}) with a 1 : 5 ratio of lithium ions to titanium ions and 32e sites are occupied by oxygen.^{3,4} The octahedral 16c sites and the tetrahedral 8b and 48f sites are vacant which simplifies the intercalation and de-intercalation of lithium ions into the structure of LTO. This process accommodates up to three lithium ions as per eqn (6) shown above. The transfer of lithium ions causes the phase of LTO to change from the spinel ($\text{Li}_4\text{Ti}_5\text{O}_{12}$) to rock-salt phase ($\text{Li}_7\text{Ti}_5\text{O}_{12}$). Three lithium atoms at the 8a sites move during discharge to 16c sites and the inserted lithium ions occupy the vacant sites, this process is reversed during charge operation. The lithium ion diffusivity of the spinel phase is higher than that of the rock-salt phase because of the full occupancy of lithium sites in the rock-salt phase while the electronic conductivity of the rock-salt phase is higher because the Ti oxidation state in the spinel phase is +4 which limits its electronic conductivity while the average oxidation state of Ti in the rock-salt phase is +3.4 due to the existence of both Ti^{3+} (60%) and Ti^{4+} (40%).⁴⁸

The nickel insertion and the formation of $\text{Li}_4\text{Ti}_{5-x}\text{Ni}_x\text{O}_{12}$ ($x = 0.05$ and 0.1) and the change in the valence state of Ti ions from Ti^{4+} to Ti^{3+} confirmed by XPS results have positively affected the lithium transfer process and enhanced the efficiency with which LTO is utilized for Li^+ storage by making the entire LTO material accessible for intercalation leading to higher initial capacity. The dual improvement in electronic conductivity due to nickel doping and improved lithium diffusivity in well crystallized 1D nanofiber morphology with good strain relaxation, shorter distance for Li^+ diffusion, interfacial control, continuous electron transport pathways and structural stability^{49,50} further improved the thermodynamics of lithium intercalation reactions because nickel is well distributed across all the LTO structures as shown in the TEM image which not only enhanced and accelerated the intercalation/de-intercalation process of Li^+ ions, but also helped LTO to maintain fast lithium ion diffusion kinetics at high current rates leading to excellent capacity at high power rates as the LIB anode material and outstanding energy densities at high power densities in asymmetric hybrid supercapacitors. The improved results of Ni-LTONF₁₀ compared to LTONF₅ can be attributed to the additional amount of nickel which further improved the LTO initial capacity and lithium intercalation thermodynamics.

Materials

All materials were purchased from Sigma Aldrich and used without further purifications.

Experimental setup

The electrospinning technique shown in Fig. 12 has been utilized to produce nickel doped 1-D lithium titanate nanofibers ($\text{Li}_4\text{Ti}_{5-x}\text{Ni}_x\text{O}_{12}$) using titanium(IV) isopropoxide, lithium acetate, nickel acetate and poly-vinylpyrrolidone (PVP) as the precursors.

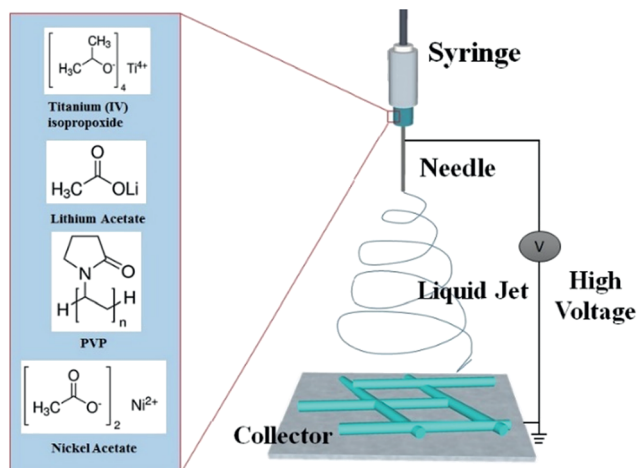


Fig. 12 Electrospinning experimental setup.

Synthesis of LTO nanofibers

0.95 g titanium(IV) isopropoxide ($\text{Ti}[\text{OCH}(\text{CH}_3)_2]_4$), 0.1855 g lithium acetate dihydrate ($\text{LiC}_2\text{H}_3\text{O}_2 \cdot 2\text{H}_2\text{O}$), and 0.51 g polyvinylpyrrolidone (PVP, MW = 1.3 M) were all added to a vial containing 8.5 ml pure ethanol and 2.5 ml acetic acid. The solution was stirred for 6 hours on a hot plate at 35 °C and 1150 rpm. The precursor solution was then moved to a 14.1 mm plastic syringe with a metallic needle attached to a high voltage source (19.0 kV). The needle tip was placed 14.5 cm from an aluminum foil current collector and the flow rate was set to 0.15 ml h^{-1} . The collected fibers were moved to a quartz tube and annealed inside a tubular furnace at 780 °C in air for 5 hours (3 °C min^{-1}) to remove all organic materials. Finally, the sample was left to cool naturally before collecting the end product.

Synthesis of Ni-LTO nanofibers

Nickel doped LTO nanofibers were synthesized by adding (drop wise) an appropriate amount of nickel acetate solution dissolved in 2 ml ethanol to the precursor solution described in the LTONF synthesis. The rest of the steps followed the same procedure as LTONF synthesis. The investigated materials include pure LTO nanofibers (LTONFs) and two nickel to LTO molar ratios (1 : 20 and 1 : 10).

Synthesis of LTO nanoparticles

LTO nanoparticles were synthesized by combining stoichiometric amounts of lithium carbonate (Li_2CO_3) and titanium dioxide (TiO_2) in a planetary ball mill using a 125 ml grinding jar and zirconium balls. The material was ball milled for 12 hours under 300 RPM. The resulting fine powder was then heat-treated at 780 °C in air to produce LTO nanoparticles.

Morphological and structural characterization

The crystal structure of the samples was characterized using an X-ray diffractometer (XRD, RIETVELDXRG 3000) and an X-ray photoelectron spectrometer (XPS, PHI Quantera) located at the Ontario Center for Characterization of Advanced Materials

(University of Toronto). BET analysis was performed after samples were degassed at 200 °C for two hours under vacuum. 2D Raman mapping was performed using a Senterra 2 Bruker Raman instrument. Sample morphology was examined using a scanning electron microscope (SEM, ZEISS ULTRA PLUS), a Raman spectrometer (SENTERRA 314) and a transmission electron microscope (TEM, JEOL 2010F TEM/STEM field emission microscope) at the Canadian center for electron microscopy (CCEM) located at McMaster University.

Cell fabrication

The electrochemical tests of LIBs were conducted by fabricating the electrode materials into coin cells. Each coin cell was made of a working electrode, a separator and a lithium foil electrode in an organic electrolyte medium. The working electrode was prepared by mixing the synthesized material with carbon black (super P) using a mortar and pestle for 30 minutes. A polyvinylidene fluoride (PVDF) binder was then added, and the mixture was ground again for 20 minutes. The ratio of the synthesized material, super P, and PVDF was 80 : 10 : 10. The *N*-methyl-pyrrolidone (NMP) solvent was added to make a slurry which was coated on a 1 cm^2 copper current collector. The loading for all electrodes was approximately 1.0 mg cm^{-2} . The coated electrodes were dried at 80 °C for 2 hours followed by overnight drying in a vacuum oven at 110 °C in order to remove all the NMP solvents.

The HSC cells were fabricated with the Ni-LTONF₁₀ material as the anode, a separator and commercial activated carbon (AC) as the cathode. The anodic electrode of the HSC was prepared using 80 wt% active material, 10 wt% carbon black, and 10 wt% PVDF binder.

Coin cells for both LIBs and HSCs were assembled in a glovebox filled with argon. 1 M lithium hexafluorophosphate (LiPF_6) in ethylene carbonate and dimethyl carbonate (EC-DMC 1 : 1 volume) was used as the electrolyte.

Conclusion

As a conclusion, dual improvement of LTO properties was achieved through *in situ* nickel doping into 1D lithium titanate nanofibers synthesized by a facile electrospinning technique. The nickel insertion changed the chemical composition of LTO nanofibers without affecting the spinel crystal structure. The doped LTO nanofibers show improved capacity and outstanding rate capability at high power rates. The 10% nickel doped LTO nanofiber material showed an initial capacity of 190 mA h g^{-1} and 63 mA h g^{-1} at 50C with a smaller voltage gap between the oxidation and reduction peaks compared to the LTONF and Ni-LTONF₅. The hybridization of the 10% doped material into the asymmetric supercapacitor also showed improved energy density at high power rates. Characterization techniques confirmed the homogenous distribution of nickel into the structure of LTO without affecting the crystal structure or a noticeable effect on the LTO lattice size. The 1D longitudinal nanofiber morphology is obtained in both doped and un-doped LTONFs with some increase in the nanofiber

diameters in nickel doped LTONFs. The characterization techniques also confirmed the stable nanofiber morphology after long-term cycling.

References

- 1 G.-N. Zhu, Y.-G. Wang and Y.-Y. Xia, *Energy Environ. Sci.*, 2012, **5**, 6652–6667.
- 2 Z. Ding, L. Zhao, L. Suo, Y. Jiao, S. Meng, Y.-S. Hu, Z. Wang and L. Chen, *Phys. Chem. Chem. Phys.*, 2011, **13**, 15127–15133.
- 3 T.-F. Yi, S.-Y. Yang and Y. Xie, *J. Mater. Chem. A*, 2015, **3**, 5750–5777.
- 4 X. Sun, P. V. Radovanovic and B. Cui, *New J. Chem.*, 2014, **39**, 38–63.
- 5 B. Zhao, R. Ran, M. Liu and Z. Shao, *Mater. Sci. Eng., R*, 2015, **98**, 1–71.
- 6 Y.-M. Jiang, K.-X. Wang, H.-J. Zhang, J.-F. Wang and J.-S. Chen, *Sci. Rep.*, 2013, **3**, 3490.
- 7 T.-F. Yi, L.-J. Jiang, J. Shu, C.-B. Yue, R.-S. Zhu and H.-B. Qiao, *J. Phys. Chem. Solids*, 2010, **71**, 1236–1242.
- 8 J.-G. Kim, D. Shi, M.-S. Park, G. Jeong, Y.-U. Heo, M. Seo, Y.-J. Kim, J. Kim and S. Dou, *Nano Res.*, 2013, **6**, 365–372.
- 9 B. Zhang, Z.-D. Huang, S. W. Oh and J.-K. Kim, *J. Power Sources*, 2011, **196**, 10692–10697.
- 10 X. Li, M. Qu, Y. Huai and Z. Yu, *Electrochim. Acta*, 2010, **55**, 2978–2982.
- 11 H. Wu, S. Chang, X. Liu, L. Yu, G. Wang, D. Cao, Y. Zhang, B. Yang and P. She, *Solid State Ionics*, 2013, **232**, 13–18.
- 12 H. Zhao, Y. Li, Z. Zhu, J. Lin, Z. Tian and R. Wang, *Electrochim. Acta*, 2008, **53**, 7079–7083.
- 13 S. Huang, Z. Wen, X. Zhu and Z. Lin, *J. Power Sources*, 2007, **165**, 408–412.
- 14 Y. K. Sun, D. J. Jung, Y. S. Lee and K. S. Nahm, *J. Power Sources*, 2004, **125**, 242–245.
- 15 H. Song, S.-W. Yun, H.-H. Chun, M.-G. Kim, K. Y. Chung, H. S. Kim, B.-W. Cho and Y.-T. Kim, *Energy Environ. Sci.*, 2012, **5**, 9903–9913.
- 16 J.-G. Kim, M.-S. Park, S. M. Hwang, Y.-U. Heo, T. Liao, Z. Sun, J. H. Park, K. J. Kim, G. Jeong, Y.-J. Kim, J. H. Kim and S. X. Dou, *ChemSusChem*, 2014, **7**, 1451–1457.
- 17 Y.-J. Hao, Q.-Y. Lai, J.-Z. Lu and X.-Y. Ji, *Ionics*, 2007, **13**, 369–373.
- 18 J. Kim, S.-W. Kim, H. Gwon, W.-S. Yoon and K. Kang, *Electrochim. Acta*, 2009, **54**, 5914–5918.
- 19 C. Lin, M. O. Lai, L. Lu, H. Zhou and Y. Xin, *J. Power Sources*, 2013, **244**, 272–279.
- 20 W. Long, X. Wang, S. Yang, H. Shu, Q. Wu, Y. Bai and L. Bai, *Mater. Chem. Phys.*, 2011, **131**, 431–435.
- 21 M. S. Wilm and M. Mann, *Int. J. Mass Spectrom. Ion Processes*, 1994, **136**, 167–180.
- 22 J. Wu, N. Wang, Y. Zhao and L. Jiang, *J. Mater. Chem. A*, 2013, **1**, 7290–7305.
- 23 B. Zhang, F. Kang, J.-M. Tarascon and J.-K. Kim, *Prog. Mater. Sci.*, 2016, **76**, 319–380.
- 24 P. Gupta, C. Elkins, T. E. Long and G. L. Wilkes, *Polymer*, 2005, **46**, 4799–4810.
- 25 F. Wu, X. Li, Z. Wang and H. Guo, *Ceram. Int.*, 2014, **40**, 13195–13204.
- 26 J. Wolfenstine and J. L. Allen, *J. Power Sources*, 2008, **180**, 582–585.
- 27 L. Cheng, J. Yan, G.-N. Zhu, J.-Y. Luo, C.-X. Wang and Y.-Y. Xia, *J. Mater. Chem.*, 2010, **20**, 595–602.
- 28 M. R. Jo, Y. S. Jung and Y.-M. Kang, *Nanoscale*, 2012, **4**, 6870–6875.
- 29 V. Aravindan, J. Sundaramurthy, P. Suresh Kumar, Y.-S. Lee, S. Ramakrishna and S. Madhavi, *Chem. Commun.*, 2015, **51**, 2225–2234.
- 30 H. Li, L. Shen, B. Ding, G. Pang, H. Dou and X. Zhang, *Nano Energy*, 2015, **13**, 18–27.
- 31 J. G. Kim, M. S. Park, S. M. Hwang, Y. U. Heo, T. Liao, Z. Sun, J. H. Park, K. J. Kim, G. Jeong, Y. J. Kim, J. H. Kim and S. X. Dou, *ChemSusChem*, 2014, **7**, 1451–1457.
- 32 J.-W. Jung, C.-L. Lee, S. Yu and I.-D. Kim, *J. Mater. Chem. A*, 2016, **4**, 703–750.
- 33 C. J. Angamma and S. H. Jayaram, *IEEE Trans. Ind. Appl.*, 2011, **47**, 1109–1117.
- 34 B. Sun, Y. Z. Long, H. D. Zhang, M. M. Li, J. L. Duvail, X. Y. Jiang and H. L. Yin, *Prog. Polym. Sci.*, 2014, **39**, 862–890.
- 35 T. D. Tran, J. H. Feikert, X. Song and K. Kinoshita, *J. Electrochem. Soc.*, 1995, **142**, 3297–3302.
- 36 Y. Shen, M. Søndergaard, M. Christensen, S. Birgisson and B. B. Iversen, *Chem. Mater.*, 2014, **26**, 3679–3686.
- 37 K. Zaghbi, M. Simoneau, M. Armand and M. Gauthier, *J. Power Sources*, 1999, **81–82**, 300–305.
- 38 Y.-R. Jhan and J.-G. Duh, *Electrochim. Acta*, 2012, **63**, 9–15.
- 39 D. Capsoni, M. Bini, V. Massarotti, P. Mustarelli, G. Chiodelli, C. B. Azzoni, M. C. Mozzati, L. Linati and S. Ferrari, *Chem. Mater.*, 2008, **20**, 4291–4298.
- 40 D.-D. Han, G.-L. Pan, S. Liu and X.-P. Gao, *RSC Adv.*, 2015, **5**, 92354–92360.
- 41 F. Li, M. Zeng, J. Li, X. Tong and H. Xu, *RSC Adv.*, 2016, **6**, 26902–26907.
- 42 S. Huang, Z. Wen, Z. Gu and X. Zhu, *Electrochim. Acta*, 2005, **50**, 4057–4062.
- 43 S. Ganapathy, E. R. H. van Eck, A. P. M. Kentgens, F. M. Mulder and M. Wagemaker, *Chem.–Eur. J.*, 2011, **17**, 14811–14816.
- 44 Z. Yu, X. Zhang, G. Yang, J. Liu, J. Wang, R. Wang and J. Zhang, *Electrochim. Acta*, 2011, **56**, 8611–8617.
- 45 J. Jamnik and J. Maier, *J. Electrochem. Soc.*, 1999, **146**, 4183–4188.
- 46 T. Chen and L. Dai, *J. Mater. Chem. A*, 2014, **2**, 10756–10775.
- 47 S. Roldán, D. Barreda, M. Granda, R. Menéndez, R. Santamaría and C. Blanco, *Phys. Chem. Chem. Phys.*, 2014, **17**, 1084–1092.
- 48 D. Liu, C. Ouyang, J. Shu, J. Jiang, Z. Wang and L. Chen, *Phys. Status Solidi B*, 2006, **243**, 1835–1841.
- 49 C. K. Chan, H. Peng, G. Liu, K. McIlwrath, X. F. Zhang, R. A. Huggins and Y. Cui, *Nat. Nanotechnol.*, 2008, **3**, 31–35.
- 50 L. Mai, Y. Dong, L. Xu and C. Han, *Nano Lett.*, 2010, **10**, 4273–4278.